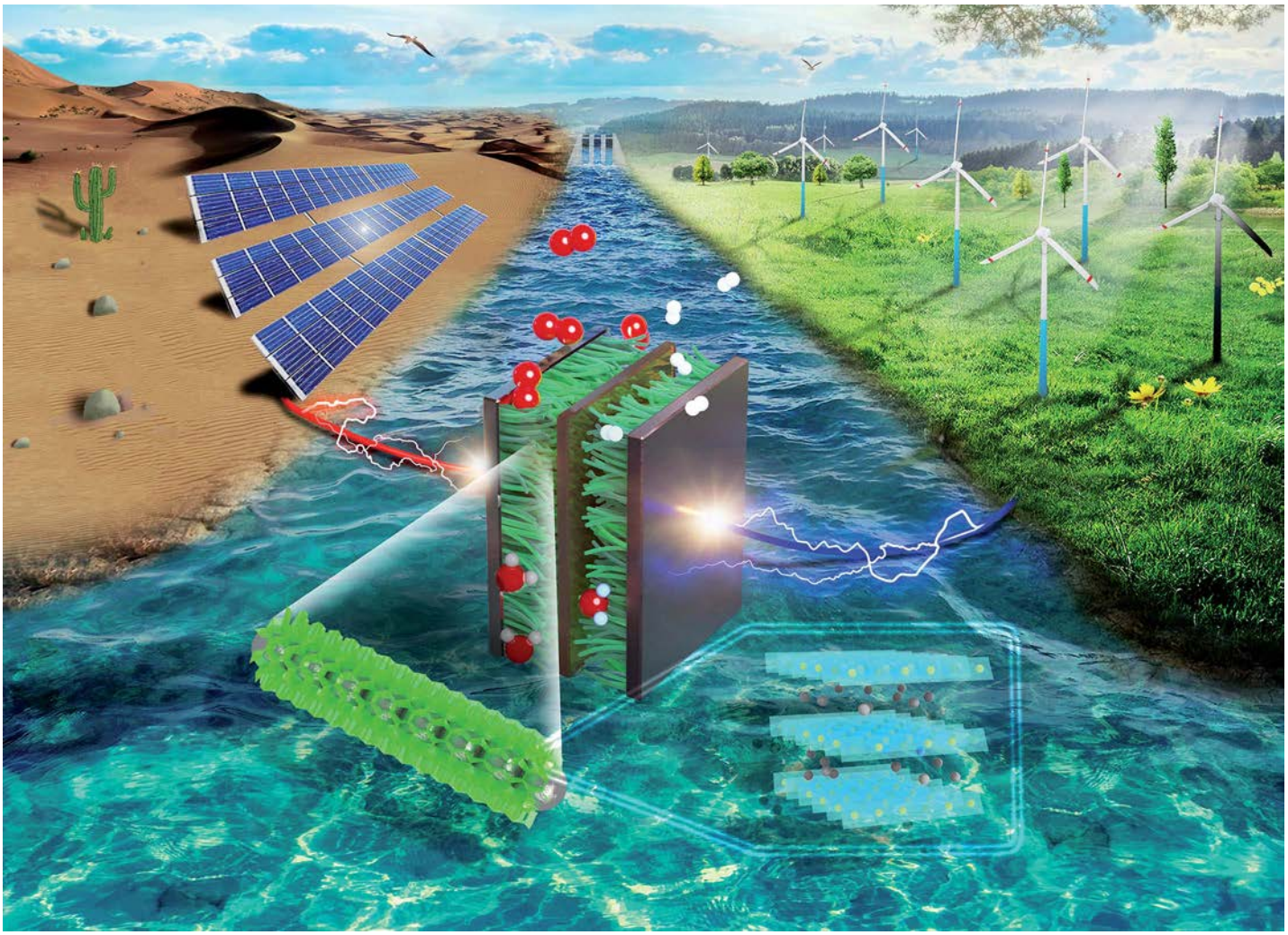

Showcasing joint research from the laboratories of Dr Ping Wang & Dr XianYing Wang at School of Materials Science and Technology, University of Shanghai for Science and Technology, Shanghai, P. R. China and Dr Johnny C. Ho at Department of Materials Science and Engineering, City University of Hong Kong, Hong Kong, P. R. China.

Simple and cost effective fabrication of 3D porous core–shell Ni nanochains@NiFe layered double hydroxide nanosheet bifunctional electrocatalysts for overall water splitting

By integration into high-performance electrolytic overall-water-splitting cell packs, meticulously designed nanoarchitecture of 3D porous core-shell Ni nanochains@NiFe layered double hydroxide nanosheet bifunctional electrocatalysts with excellent overall water splitting performance will open up a potential key storage way for a highly renewable and efficient power system.

As featured in:

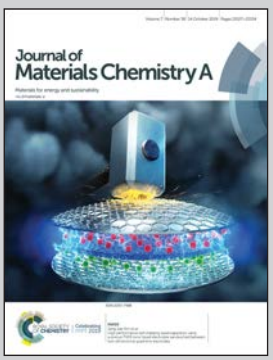

See Ping Wang, Johnny C. Ho, Xianying Wang *et al.*, *J. Mater. Chem. A*, 2019, **7**, 21722.

ROYAL SOCIETY OF CHEMISTRY | Celebrating IYPT 2019

rsc.li/materials-a

Registered charity number: 207890

Journal of Materials Chemistry A

PAPER

View Article Online
View Journal | View Issue

Check for updates

Cite this: J. Mater. Chem. A, 2019, 7, 21722

Simple and cost effective fabrication of 3D porous core–shell Ni nanochains@NiFe layered double hydroxide nanosheet bifunctional electrocatalysts for overall water splitting†

Zhengyang Cai, ‡[a] Xiuming Bu,‡[b] Ping Wang, *[ac] Wenqiang Su,[a] Renjie Wei, [b] Johnny C. Ho, *[b] Junhe Yang[ac] and Xianying Wang*[ac]

Highly efficient, durable and cost-effective electrocatalysts are highly desired for overall water splitting (OWS). Herein, we report the easy fabrication of 3D porous core–shell Ni nanochains@NiFe layered double hydroxide (LDH) nanosheets with extraordinary oxygen evolution reaction (OER), hydrogen evolution reaction (HER) and OWS performance. In specific, a simple magnetic field-assisted method is used for the *in situ* growth of Ni nanochain cores with large surface areas, allowing the subsequent vertical growth of few-layered NiFe LDH nanosheets to form densely packed shells. Benefiting from the meticulously designed nanoarchitecture, the electrocatalyst possesses rich exposed active sites, plentiful charge transfer channels and high porosity for the release of gas bubbles. The OER performance and durability of the electrocatalyst are far better than those of both commercial RuO_2 and IrO_2, while its HER performance is competitive with the performance of the benchmark Pt/C electrode in alkaline electrolytes. When these catalysts are further employed as anode and cathode electrodes, small cell voltages of 1.53 and 1.78 V can be achieved at current densities of 10 and 100 mA cm^{-2} for a long-term OWS reaction. Towards the commercial use, we design an electrolytic overall-water-splitting cell pack, which demonstrates a linear relationship between the numbers of packing cells and the increase of current density under a given voltage.

Received 6th July 2019
Accepted 30th July 2019

DOI: 10.1039/c9ta07282a

rsc.li/materials-a

Published on 31 July 2019. Downloaded on 10/11/2019 5:51:56 AM.

Introduction

In the past decades, electrochemical water splitting has attracted tremendous attention as a clean and sustainable way for hydrogen production and renewable energy conversion;[1,2] however, both cathodic hydrogen evolution reaction (HER) and anodic oxygen evolution reaction (OER) are still not efficient enough to support the overall water splitting (OWS). In general, OER is the major bottleneck of the uphill OWS, particularly due to the high activation barrier and the sluggish four proton-coupled electron transfer.[3–5] Although many noble metals are widely employed as electrocatalysts, such as Pt-group materials for HER and Ru/Ir-based materials for OER, the required overpotentials to achieve high current densities (*e.g.* 100 and 500 mA cm^{-2}) are inevitably quite large. Importantly, the pH-dependent performance of HER and OER imposes another substantial challenge such that the system integration into the same electrolyte being inaccessible.[6–8] As a result, the low earth abundance of noble metals and the high cost associated with the inefficient system integration would strictly limit the practical utilization of large-scale water electrolysis.[9,10]

Until now, significant research has been devoted to developing efficient and low-cost bifunctional electrocatalysts for OWS, including transition metal-based (Ni, Co and Fe) catalysts and others.[11–16] Taking advantage of their unique 2D layered structure, transition metal-based layered double hydroxide (LDH) nanosheets are considered as one of the promising bifunctional electrocatalysts for OWS.[17–24] It is noted that the exposure of catalytically active sites of these 2D nanosheets is much more intensive as compared to those of the 0D and 1D structures, in which the diffusion of water molecules and release of gaseous products can be accelerated. In addition, the relatively low cost and ease of large-area fabrication of these LDH nanosheets would make them attractive for large-scale applications. For example, Song and Hu studied the OER activities of bulk and exfoliated CoCo, NiCo and NiFe LDHs, where it was demonstrated that the single-layer LDH

[a]School of Materials Science and Technology, University of Shanghai for Science and Technology, Jungong Rd. 516, 200093 Shanghai, P. R. China. E-mail: ping.wang@usst.edu.cn; xianyingwang@usst.edu.cn

[b]Department of Materials Science and Engineering, City University of Hong Kong, 83 Tat Chee Avenue, Kowloon, Hong Kong, P. R. China. E-mail: johnnyho@cityu.edu.hk

[c]Shanghai Innovation Institute for Materials, 200444 Shanghai, P. R. China

† Electronic supplementary information (ESI) available: Experimental details and results. See DOI: 10.1039/c9ta07282a

‡ These authors contributed equally to the work.

This journal is © The Royal Society of Chemistry 2019

Published on 31 July 2019. Downloaded on 10/11/2019 5:51:56 AM.

nanosheets had increased active site density, higher conductivity and greater activity than the bulk ones.[25] Nevertheless, for these exfoliated LDHs, the use of conductive adhesives (*e.g.* Nafion polymer binder) was required for the conductivity improvement, which would give rise to an increase of the associated ohmic drop. Besides that, the complicated and slow-throughput exfoliation process would greatly restrict the deployment of those LDHs for industrial use.[26]

The design of 3D core–shell structured LDHs self-supported on conductive substrates is of great interest both from scientific and practical points of view. Also, we have witnessed great successes in the electrocatalytic applications of 3D core–shell structured LDHs.[23,27–31] For instance, Feng *et al.* developed Co@FeOOH core–shell nanotube arrays supported on Ni foams as 3D self-standing electrodes for OER.[27] The inner Co metallic cores could serve as the highly conductive layer to facilitate reliable electron transfer and to improve the electrical conductivity of FeOOH. The energy barriers of intermediates were then decreased accordingly, which promoted the corresponding catalytic reactions. However, they commonly suffer from the complex multi-step synthesis procedure, which could hardly meet the practical requirements. Furthermore, there are still many substantial challenges needed to be tackled in order to utilize these 3D core–shell structured LDH catalysts. These challenges include four main areas as listed as follows: (i) Precisely controlling the structure of LDHs, such as achieving more uniformly aligned LDH nanoarrays, hierarchically porous LDH nanosheets, and ultrathin few-layer LDHs. (ii) Optimizing the quantity of active sites in LDH materials. It is necessary to unambiguously clarify the possible origins of these active sites, which reduce the energy barrier of the rate-determining step during chemical reactions. It is also important to elucidate the catalytic mechanism of LDH-based electrocatalysts for water splitting at the atomic or molecular level. (iii) Optimizing the conductivity of the supports of LDHs. (iv) Decoupling the performance dependence of most LDHs on alkaline electrolytes. These alkaline media can cause severe corrosion of electrodes and cell components; therefore, a long-term durability of these LDH materials in electrolytes must be considered.

Herein, we design and successfully fabricate Ni nanochains (NCs)@NiFe LDH nanosheet (NS) bifunctional catalysts (denoted as Ni@NiFe LDH) with a 3D porous core–shell architecture for highly efficient OER, HER and OWS. To be specific, the obtained electrode exhibits outstanding OER performances with a small Tafel slope of 66.3 mV dec^{-1}, which gives low overpotentials of 218, 269 and 315 mV at current densities of 10, 100, and 300 mA cm^{-2}, respectively. For HER, the electrode also yields remarkably low overpotentials of 92 and 233 mV at current densities of 10 and 100 mA cm^{-2}, accordingly. It is important that when these Ni@NiFe LDH electrodes are configured as both the anode and cathode in a single cell, adequately small cell voltages of 1.53 and 1.78 V at current densities of 10 and 100 mA cm^{-2} are observed for OWS. These superior OWS performances exceed those of the state-of-the-art IrO_2 (+)//Pt/C (−) electrodes (1.55 and 1.84 V). Even after the stability test for 24 h, there is only a negligible increase of 38 mV in the cell voltage. These excellent electrocatalytic characteristics and durability of Ni@NiFe LDH NSs are mainly attributed to the superiority of the 3D porous core–shell structure. This unique structure does not only offer a large surface area, enabling the generation of abundant active sites and mass transfer channels, but also facilitates the release of gas molecules. The *in situ* growth of Ni NC cores on Ni foam can also firmly hold the NiFe LDH shells, ensuring good electron-transfer ability and structural stability. In this case, the formation of few-layered NiFe LDH NSs can cause the active edge sites to be fully exposed for efficient catalytic reactions.

Results and discussion

Fig. 1 illustrates the fabrication procedure of the 3D porous core–shell Ni@NiFe LDH nanocomposite, which comprises only two simple steps. Firstly, vertical Ni NCs are grown directly on the Ni foam substrate (cross-sectional view in Fig. S1d and e†) by a modified magnetic field-assisted chemical reduction method. As compared with the multi-step and complicated synthesis procedure of metallic nanowires as cores, such as Co[27] or Cu,[29] the one step *in situ* growth of Ni NCs cores in our work is much more easier and controllable on the conductive Ni foam substrate. Subsequently, the NiFe LDH catalysts are electrodeposited onto the self-supported Ni NCs within less than a minute. As shown in the optical images (Fig. S1a–c†), there is an obvious color change associated with the as-synthesized samples taken right after different steps, indicating the

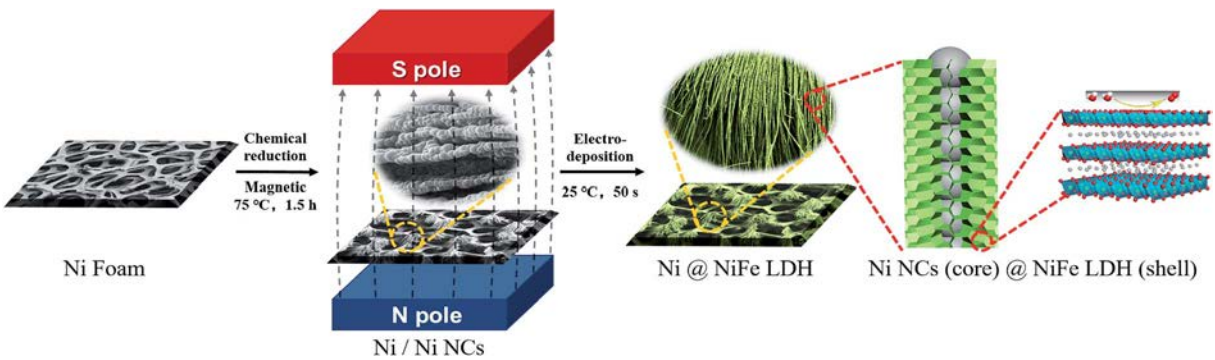

Fig. 1 Schematic illustration of the fabrication procedure of self-supported 3D porous core–shell Ni@NiFe LDH.

Published on 31 July 2019. Downloaded on 10/11/2019 5:51:56 AM.

successful formation of yellow-green colored and uniform Ni@NiFe LDHs. The uniform growth of Ni NCs on Ni foam is shown in the top view of Fig. S1d.† It is worth mentioning that the entire preparation process can be completed in a relatively short time (<2 h), while all the reactions take place at room temperature without utilizing any high-temperature treatment. In this regard, this fabrication method can be considered as a cost-effective and easy route for many industrial scale applications.

Scanning electron microscopy (SEM) and transmission electron microscopy (TEM) are employed to evaluate the morphology and to verify the core–shell nanostructure of as-synthesized samples. The representative SEM image of the rough Ni foam is presented in Fig. S2a.† Fig. S3† shows the SEM images of ultrathin and homogeneous NiFe LDH NSs directly electrodeposited on Ni foam over the NiFe LDH sample. Importantly, Fig. 2a and b show the low-magnification and high-magnification SEM images of the obtained Ni NCs, respectively. The Ni NCs mainly composed of reduced Ni nanoparticles possess a bead-chain-like structure and grow uniformly on Ni foam. However, without the employment of the magnetic field, only the formation of reduced Ni nanoparticles is observed on the surface of the Ni foam (Fig. S2b and c†), instead of *in situ* growth of Ni NCs. As presented in Fig. 2c, vertically standing NiFe LDH nanosheets are distributed homogenously and densely on the surface of Ni NCs and a 3D porous core–shell architecture is indeed formed, which would greatly facilitate the electrolyte diffusion and release of gas products.[23,29] Fig. S4† presents the influence of electrodeposition time on the morphology of the obtained products. With the optimal electrodeposition time of 50 s, the most uniform distribution of NiFe LDH nanosheets is obtained. A shorter electrodeposition time of 10 s will cause an insufficient coverage of Ni NCs, giving rise to a serious loss of the effective surface area, while an extended time of 90 s would result in agglomerated LDH nanospheres with a size of 300 to 360 nm, which would be detrimental for charge conduction and exposure of active sites. The argon adsorption/desorption measurement was carried out to determine the surface area and porous structure of the Ni@NiFe LDH electrodes, according to the Brunauer–Emmett–Teller (BET) method. Fig. S5† presents the argon adsorption/desorption isotherm curves of the Ni@NiFe LDH, showing the characteristic of the porous structure.[32] The BET surface area of Ni@NiFe LDH was greatly enhanced to be about 6.5 $m^2 g^{-1}$ (normalized by the total mass of the electrode: 37.9 mg), compared with that of commercial Ni foams (1.9 $m^2 g^{-1}$). Taking the amount of active NiFe LDH (2.3 mg) into consideration, the specific surface area of NiFe LDH reaches up to 106.5 $m^2 g^{-1}$. The inset in Fig. S5† displays pore size distribution measured from the adsorption isotherm branch using the Barrett–Joyner–Halenda (BJH) method. The pore size distribution of the Ni@NiFe LDH is mainly centered in the range of 2–10 nm. In order to evidently confirm the 3D porous core–shell structure, detailed TEM studies are performed and the images are shown in Fig. 2d–f. It is clear that the structure is composed of Ni NC cores with diameters in the range of 500 to 900 nm and NiFe LDH NS shells with a thickness of around 90 nm. The average layer thickness of the NiFe LDH NSs can be estimated to be about 10 nm, which is equal to 12 atomic layers.[25] Such a 3D porous core–shell architecture can enlarge the surface area and provide abundant active edge sites and improve charge transport at the nanoscale. The well-resolved high-resolution TEM (HRTEM) image in Fig. 2f further reveals lattice fringes with a spacing distance of ~0.25 nm, corresponding to the (012) plane of NiFe LDH.[19] The energy dispersive X-ray spectroscopy (EDX) results in Fig. 2g and h can again confirm the core–shell nanostructure, where the inner core is composed of Ni elements and the LDH shell contains uniformly distributed Ni and Fe elemental components.

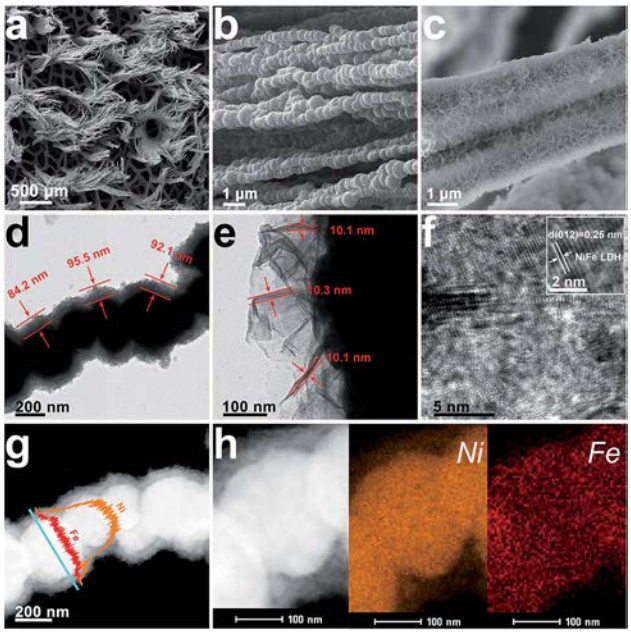

Fig. 2 Representative SEM images of Ni NCs at low (a) and high (b) magnification, SEM images of Ni@NiFe LDH (c), TEM images of Ni@NiFe LDH (d and e), HRTEM image of Ni@NiFe LDH (f), the inset shows the corresponding lattice fringe of the (012) crystal facet in NiFe LDH, EDS line scans (g), and DF-STEM image of Ni@NiFe LDH with the corresponding elemental mappings of Ni and Fe (h).

The powder X-ray diffraction (XRD) patterns of the Ni NCs and Ni@NiFe LDH are shown in Fig. 3a. Two sharp diffraction peaks located at 44.51° and 51.84° can be assigned to the cubic-structured Ni (JCPDS no. 04-0850) and no other diffraction peaks are observed, indicating the complete reduction of Ni NCs. After the electrodeposition process, intense diffraction peaks of the (003), (012), (110) and (113) planes of the NiFe LDHs can be clearly observed at 11.5°, 34.8°, 60.4° and 61.5°, which are in accordance with the corresponding standard card (JCPDS no. 51-0463).[17,33] The Raman spectra of the Ni@NiFe LDH before and after OER are shown in Fig. S6a.† Before the OER test, two main Raman peaks located at 453 cm^{-1} and 527 cm^{-1} can be assigned to the Ni hydroxide and Fe oxyhydroxide species.[19,34] After the OER test run and stability test for 24 h, the same peaks located at 475 cm^{-1} and 552 cm^{-1} can be attributed to the OER active phase of γ-NiOOH, which is in

 This journal is © The Royal Society of Chemistry 2019

Published on 31 July 2019. Downloaded on 10/11/2019 5:51:56 AM.

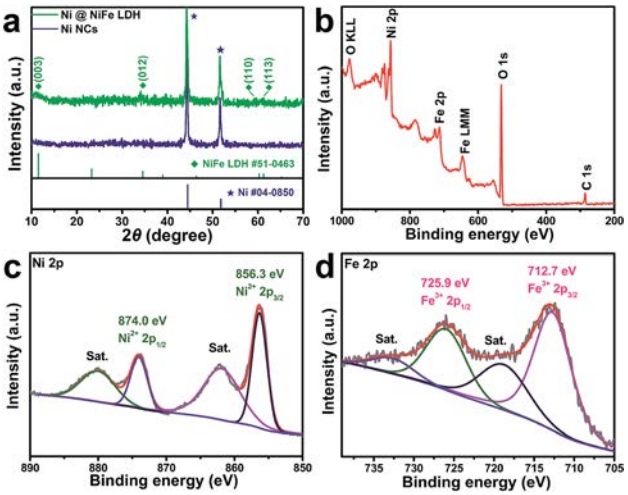

Fig. 3 (a) XRD patterns of Ni NCs and Ni@NiFe LDH. (b) Wide-scan XPS spectra and high-resolution XPS spectra of (c) Ni 2p and (d) Fe 2p for Ni@NiFe LDH.

good agreement with the literature.[19,33,34] As shown in Fig. S6b,† the FTIR spectrum of the Ni@NiFe LDH after the OER test shows that the bands at around 600 cm^{-1} are related to the metal–oxygen–metal lattice vibrations of the layer cations of NiFe LDH,[35,36] The stretching modes of the hydroxyl groups,[37,38] the bending modes of free water molecules[19] and antisymmetric stretching vibration of nitrate anions[35,39] are also observed, which are located at 3400–3600, 1636.3 and 1384.2 cm^{-1}, respectively. The X-ray photoelectron spectroscopy (XPS) measurements are also carried out to study the surface elemental composition as well as the oxidation states. As displayed in the wide-scan XPS spectrum in Fig. 3b, the existence of Ni, Fe, C, and O elements is obviously demonstrated in Ni@NiFe LDHs. The binding energies at 856.3 eV and 874.0 eV along with their shake-up satellites peaks at 861.9 eV and 880.0 eV are attributed to Ni $2p_{3/2}$ and Ni $2p_{1/2}$, respectively (Fig. 3c), indicating that there is only one chemical state of Ni^{2+} species.[40] Similarly, the deconvoluted Fe 2p peak comprises Fe $2p_{3/2}$ and Fe $2p_{1/2}$ spin–orbit peaks at 712.7 eV and 725.9 eV with the corresponding shake-up satellites at 718.8 eV and 732.6 eV, respectively.[41] This implies the oxidation state of Fe^{3+} (0d).[19] All these results can clearly confirm the chemical composition, morphology and core–shell architecture of the Ni@NiFe LDHs.

Apart from the material characterization, Fig. S6c† presents the OER performance assessments of Ni foam, Ni NCs, and Ni@NiFe LDH electrodes with different electrodeposition times in 1 M KOH aqueous electrolyte using a standard three-electrode system. The Ni@NiFe LDH with an electrodeposition time of 50 s (denoted as Ni@NiFe LDH hereafter) exhibits the best OER activity, which can be attributed to the optimized nanoarchitecture as discussed above. Notably, to eliminate the interference of Ni^{2+}/Ni^{3+} redox potential at around 1.43 V *vs.* RHE,[42] the cyclic voltammetry (CV) method is firstly used to measure the overpotential of the Ni@NiFe LDH (Fig. S6d†). Fig. 4a and b show the polarization curves and the corresponding Tafel slopes of the Ni@NiFe LDH, pure NiFe LDH, commercial RuO_2 and IrO_2, respectively. The OER performance is greatly enhanced on Ni@NiFe LDH, that is, the lowest overpotentials of 218 and 269 mV at current densities of 10 and 100 mA cm^{-2}, respectively. In contrast, the η_{10} and η_{100} values are observed at 239 and 310 mV for pure NiFe LDH, 246 and 355 mV for RuO_2 and 284 and 349 mV for IrO_2, respectively. We are surprised to note that higher η_{300} and even η_{500} can be realized over the Ni@NiFe LDH electrode, only requiring the overpotentials of 315 and 349 mV, respectively. Accordingly, the Ni@NiFe LDH shows the smallest Tafel slope of 66.3 mV dec^{-1}, as compared to the pure NiFe LDH (99.4 mV dec^{-1}), RuO_2 (105.3 mV dec^{-1}) and IrO_2 (67.3 mV dec^{-1}). These results suggest that the fastest OER kinetics is greatly beneficial for the inherent OER activity of Ni@NiFe LDH.[43] To further deepen the insights into the OER performance evaluation, a detailed comparison with recently reported data is given in Fig. 4f and Table S1.† In these cases, we can evidently conclude that the catalyst affords an extraordinary OER performance, outperforming many state-of-the-art noble metal-free OER catalysts in alkaline medium.

More importantly, the stability test at a constant current density of 10 mA cm^{-2} can confirm the robust electrochemical stability of the Ni@NiFe LDH for 24 h (Fig. 4c). Even after 2000 CV cycles at 10 and 100 mA cm^{-2} as demonstrated in Fig. S7,† the LSV curves show increases of only 2 and 12 mV in overpotentials, respectively, over the Ni@NiFe LDH.

To shed light on the underlying catalytic mechanism accounting for such extraordinary performances, CV measurements are performed at different scan rates from 10 to 100 mV s^{-1} (Fig. S8a–c†). The double-layer capacitance (C_{dl}) can then be determined, which is proportional to the electrochemically active surface area (ECSA). The ECSA is obtained by calculating the slope through the linear relationship between scan rates and capacitive current densities. As shown in Fig. 4d, the Ni@NiFe LDH exhibits the highest C_{dl} (8.3 mF cm^{-2}), as compared to the ones of NiFe LDH (1.3 mF cm^{-2}) and Ni foam (0.5 mF cm^{-2}). The larger C_{dl} value demonstrates an improved ECSA, suggesting that more active sites are exposed on the Ni@NiFe LDH. Next, electrochemical impedance spectroscopy (EIS) is used to measure the charge transfer resistance (R_{ct}) and series resistance (R_s) of the samples. It is demonstrated that the Ni@NiFe LDH possesses the smallest R_{ct} among the as-prepared samples (Fig. 4e). Such a small R_{ct} can point to fast electron transfer and favorable reaction kinetics, thus contributing to a small Tafel slope there.[29] In addition, from the enlarged EIS curves of the high frequency area (inset in Fig. 4e), the lowest R_s of the Ni@NiFe LDH indicates an excellent electrical contact between the NiFe LDH and Ni NCs. Undoubtedly, all these observed phenomena benefit from the advance of the direct-growth synthetic process of Ni@NiFe LDH, avoiding the use of any detrimental heating treatment. In other words, the Ni NCs are directly grown in the nodal region of Ni foam, leading to a strong adhesion. Consequently, the vertical LDHs are directly electrodeposited onto the surface of Ni NCs, ensuring structural stability and good electrical contact for the integrated structure.

Published on 31 July 2019. Downloaded on 10/11/2019 5:51:56 AM.

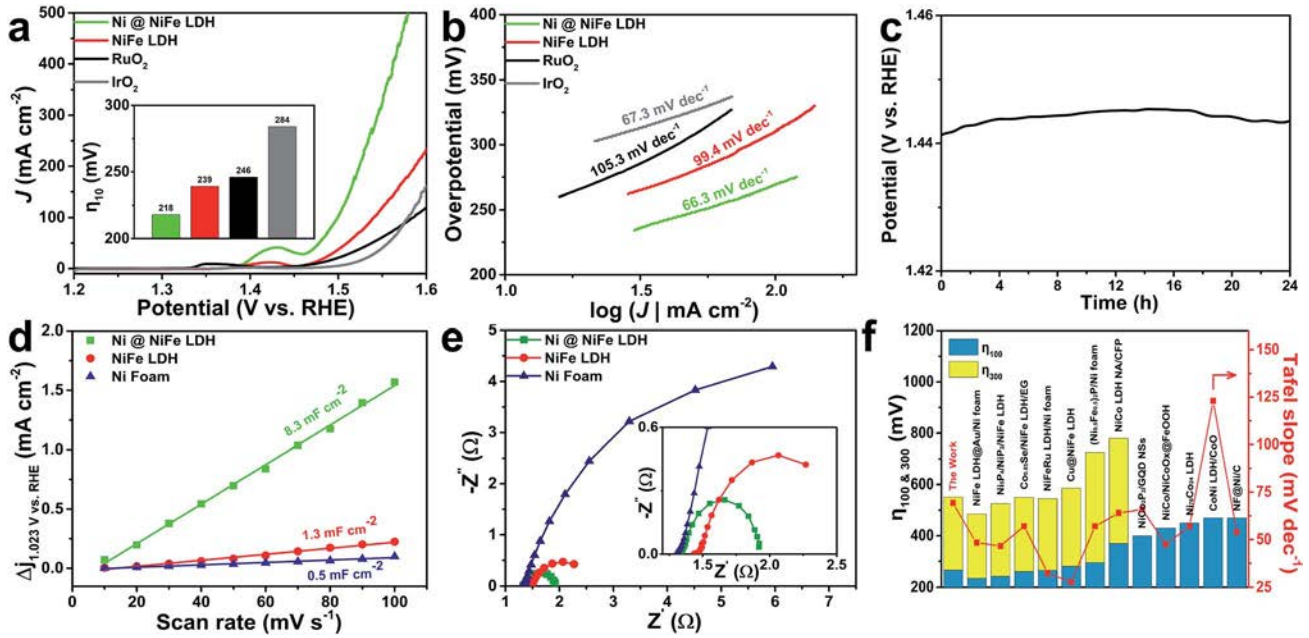

Fig. 4 OER activity measurements of the as-prepared samples in 1 M KOH aqueous electrolyte. (a) Linear sweep voltammetry (LSV) curves with a scan rate of 0.5 mV s^{-1}, the inset shows the overpotential required at 10 mA cm^{-2} (η_{10}). (b) Corresponding Tafel slopes. (c) Chronopotentiometry curves of Ni@NiFe LDH at a constant current density of 10 mA cm^{-2} (without *iR* compensation). (d) Calculations of C_{dl} for Ni@NiFe LDH, NiFe LDH and Ni foam. (e) Nyquist plots at the overpotential of 250 mV, the inset shows enlarged EIS curves. (f) Comparison of η_{100}, η_{300} and the corresponding Tafel slopes with those of other recently reported high-performance OER electrocatalysts, the corresponding references are listed in Table S1.†

On the other hand, the electrochemical HER activities of as-prepared samples are thoroughly investigated. Fig. 5a and S9† show the polarization curves of the Ni@NiFe LDH, NiFe LDH, 20 wt% Pt/C, Ni NCs and Ni foam in 1 M KOH at a scan rate of 5 mV s^{-1}. The advance of the Ni@NiFe LDH is much more obvious for high current densities. The overpotential to achieve the low current density of 10 mA cm^{-2} for Ni@NiFe LDH is about 92 mV, which is much smaller than that of NiFe LDH (216 mV) but higher than that of Pt/C (~33 mV). Interestingly, only 233 mV is required to achieve 100 mA cm^{-2} for the Ni@NiFe LDH, which is a little higher than 197 mV for the Pt/C electrode but far smaller than 336 mV for NiFe LDH. As depicted in Fig. 5b, the Ni@NiFe LDH exhibits a Tafel slope of 72.3 mV dec^{-1}, which is higher than that of the Pt/C electrode (45.2 mV dec^{-1}) but much smaller than that of NiFe LDH (163.5 mV dec^{-1}). These results show that the Volmer–Heyrovsky mechanism is responsible for HER, in which the hydrogen desorption process can be considered as the rate limiting step.[44] The Ni@NiFe LDH was also found to be stable after HER for 24 h (Fig. 5c), and only a slight increase in the overpotential required to drive a current density of 10 mA cm^{-2} was observed. Indeed, as compared to the recently reported HER electrocatalysts (Fig. 5d and Table S2†), the Ni@NiFe LDH exhibits highly competitive HER performance except for that reported by Chen *et al.*[13]

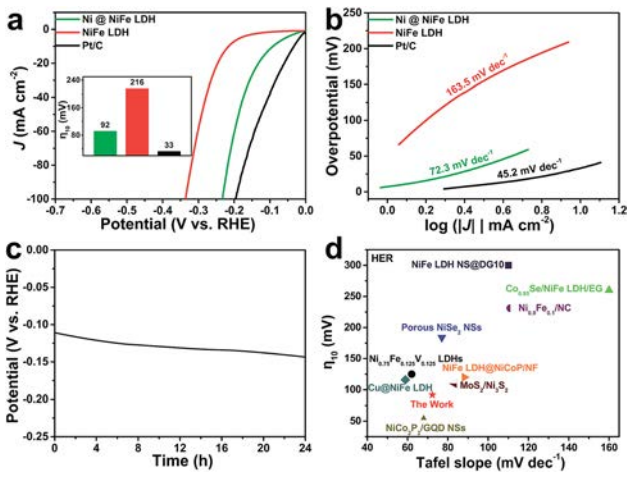

Fig. 5 HER performance of Ni@NiFe LDH in 1 M KOH aqueous solution. (a) LSV curves with a scan rate of 5 mV s^{-1}, the inset shows the overpotentials required for 10 mA cm^{-2}. (b) The corresponding Tafel plots. (c) The HER stability test of Ni@NiFe LDH at a constant current density of 10 mA cm^{-2} for 24 h (without *iR* compensation). (d) Comparison of HER performance with other recently reported HER electrocatalysts, the corresponding references are listed in Table S2.†

Based on the outstanding OER and HER activities of Ni@NiFe LDHs in the alkaline electrolyte, we further investigate the OWS ability of the Ni@NiFe LDH electrodes as both the anode and cathode in a two-electrode single cell configuration (Fig. 6a). Impressively, current densities of 10 mA cm^{-2} and 100 mA cm^{-2} are obtained at the cell voltages of 1.53 and 1.78 V over the Ni@NiFe LDH, respectively, which are smaller than those of 1.55 and 1.84 V over the IrO_2 (+)//Pt/C (−) electrodes. After maintaining at 10 mA cm^{-2} for 24 h, there is only a negligible

 This journal is © The Royal Society of Chemistry 2019

Published on 31 July 2019. Downloaded on 10/11/2019 5:51:56 AM.

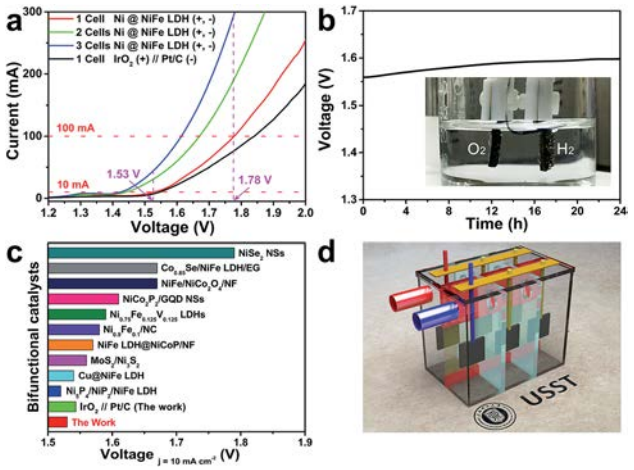

Fig. 6 OWS performance of Ni@NiFe LDH in 1 M KOH aqueous solution: (a) Polarization curves of different numbers of coupled cells, the scan rates are all kept at 5 mV s^{-1}, (b) chronopotentiometry curves of the Ni@NiFe LDH at a constant current density of 10 mA cm^{-2} in a two-electrode configuration (without *iR* compensation), the inset is the optical photograph showing the generation of O_2 and H_2 bubbles on the electrodes, (c) comparison of the required voltage at a current density of 10 mA cm^{-2} for the Ni@NiFeLDH with other recently reported bifunctional catalysts, the corresponding references are listed in Table S3,† (d) schematic of an electrolytic water-splitting cell pack for commercial and research technologies.

increase of 38 mV (equivalent to ~2.4%) in the cell voltage observed, presumably due to the dynamic process of bubble absorption on surface of the Ni@NiFe LDH electrodes.[45] These results unambiguously reveal that the catalyst possesses a very good stability (Fig. 6b). To confirm the gas evolution and faradaic efficiency of the Ni@NiFe LDH electrode, the experimental evolved amounts of H_2 and O_2 are determined by gas chromatography at a constant current density of 200 mA cm^{-2} in 1 M KOH (Fig. S10†). The measured and theoretically calculated gas amounts are observed to be in perfect agreement, suggesting a nearly 100% faradaic efficiency with the stoichiometric ratio of H_2 and O_2 being close to 2 : 1. As shown in Fig. 6c and Table S3,† the overpotential of the Ni@NiFe LDH catalyst at 10 mA cm^{-2} in 1 M KOH aqueous solution is significantly reduced, where its catalytic performance is superior to those reported by other recently developed bifunctional electrocatalysts. This substantial performance enhancement can be accounted for by the following factors: firstly, the 3D porous core–shell structure can offer a large surface area, not only enabling the generation of abundant active sites and mass transfer channels, but also facilitating the release of gas molecules during OER and HER processes. Secondly, the direct growth of Ni NC cores on Ni foam can firmly grasp the NiFe LDH NS shells, ensuring good electron-transfer ability and structural stability. Lastly, the formation of ultrathin NiFe LDH NSs down to a few layers can cause the active edge sites to be fully exposed for the catalytic reactions.

It is well known that using a single electrolytic water-splitting cell to produce H_2 and O_2 in stationary applications is limited, not only by the performance but also by the cost. The electrolytic water-splitting cell pack (EWSCP) is one of the most successful portable devices for interconversion between electrical and chemical energy; however, the use is limited to only small electronic equipment. As shown in Fig. 6d, a viable EWSCP for both commercial and research technologies is described, mainly including serially coupled cells in a parallel configuration for electrolytic water-splitting. In each cell, an ion exchange membrane is equipped in the middle of the anodic and cathodic Ni@NiFe LDH electrodes for gas separation, as well as two interconnected gas pathways separately coupled to the anodic and cathodic cells for gas extraction. To gain a fundamental understanding of the effect on electrochemical performances, EWSCPs with different numbers of coupled cells are tested, respectively (Fig. 6a). Very interestingly, a linear relationship is observed between the numbers of packing cells and the increase of current under a given voltage. In this case, the EWSCP has the unique advantage of being efficient because it is more suitable in terms of the scalability, efficiency, and weight and/or mobility of the system.

Regardless, it is important to examine the morphological and compositional variation in the recycled Ni@NiFe LDH, especially on the anode side after the OER stability test for 24 h. In this work, additional SEM, TEM, XRD and XPS characterization experiments are further carried out accordingly. As seen from the SEM images in Fig. S11,† the 3D porous core–shell structure is maintained except for the existence of a trace amount of NiFe LDH aggregated nanoparticles after the OER stability test for 24 h (Fig. S11a and b†). After the HER stability test for 24 h, the layered structure of NiFe LDH can also be well maintained without any significant peel-off phenomenon (Fig. S11d and e†). The HRTEM image in Fig. S11c† reveals an interplanar spacing of 0.25 nm, corresponding to the (012) plane of NiFe LDH, being the same as before and after the stability test (Fig. 2f). The crystalline phase of Ni@NiFe LDH is also retained, as indicated in the XRD pattern (Fig. S12a†) and Raman spectrum (Fig. S6a†). The surface chemical composition of Ni and Fe elements in the recycled sample is also measured by high-resolution XPS (Fig. S12b and c†). The Fe 2p spectrum is almost unchanged, as compared to that of the fresh sample. The atomic concentration of Ni is slightly increased from 18.4% to 19.7%, which can be ascribed to the feeble oxidation of Ni NC cores. In addition, two small new peaks at higher binding energies of 875.8 eV and 857.8 eV can be assigned to the existence of Ni^{3+}. It is probably due to the partial oxidation reaction of Ni^{2+} to form NiOOH under alkali conditions during the long-term operation, which is commonly witnessed in the literature.[42,46,47] Importantly, all these do not deteriorate the electrochemical performance of the Ni@NiFe LDH catalysts. The 3D porous core–shell Ni@NiFe LDH nanoarchitectures are evidently confirmed as highly efficient and stable bifunctional electrocatalysts toward OWS.

Conclusions

In summary, we have successfully synthesized a 3D porous core–shell structure electrocatalyst composed of *in situ* grown Ni NCs as cores and electrodeposited NiFe LDH NSs as shells. The

Published on 31 July 2019. Downloaded on 10/11/2019 5:51:56 AM.

fabricated electrode possesses a large surface area, plentiful exposed active edge sites, efficient charge and electron transfer and excellent structural stability. The corresponding electrocatalytic OER activity and durability, especially at high current densities, are far higher than the ones of commercial RuO_2 and IrO_2. This 3D porous core–shell catalyst only requires an overpotential as low as 92 mV to deliver a current density of 10 mA cm^{-2} towards HER, which is close to that of the benchmark 20 wt% Pt/C electrode (33 mV). Furthermore, a current density of 10 mA cm^{-2} at a voltage of 1.53 V with excellent durability is obtained on the electrocatalyst for OWS. Despite the high electrocatalytic performance of our 3D porous core–shell Ni@NiFe LDH catalysts for HER, OER and OWS, there is still room for further improvement. Indeed, our ongoing work will be continued on reducing the layer thickness of NiFe LDHs on an atomic scale, the feasibility of a large-size production up to the sub-meter-level with a uniform surface morphology and the design optimization and microfabrication of EWSCPs.

Conflicts of interest

There are no conflicts to declare.

Acknowledgements

We greatly appreciate the financial supports from the National Natural Science Foundation of China (51572173, 51602197, 51771121 and 51702212), Science and Technology Commission of Shanghai Municipality (16060502300, 16JC402200 and 18511110600), Innovation Program of Shanghai Municipal Education Commission (2019-01-07-00-07-E00015), Program of Shanghai Academic Research Leader (19XD1422900), Shanghai Eastern Scholar Program (QD2016014) and General Research Fund (CityU 11275961) of the Research Grants Council of Hong Kong SAR, China.

References

1 J. A. Turner, *Science*, 2004, **305**, 972–974.
2 M. Caban-Acevedo, M. L. Stone, J. R. Schmidt, J. G. Thomas, Q. Ding, H. C. Chang, M. L. Tsai, J. H. He and S. Jin, *Nat. Mater.*, 2015, **14**, 1245–1251.
3 Y. Jiao, Y. Zheng, M. Jaroniec and S. Z. Qiao, *Chem. Soc. Rev.*, 2015, **44**, 2060–2086.
4 H. Zhou, F. Yu, J. Sun, R. He, S. Chen, C. W. Chu and Z. Ren, *Proc. Natl. Acad. Sci. U. S. A.*, 2017, **114**, 5607–5611.
5 Z. Cai, X. Bu, P. Wang, J. C. Ho, J. Yang and X. Wang, *J. Mater. Chem. A*, 2019, **7**, 5069–5089.
6 S. Cherevko, S. Geiger, O. Kasian, N. Kulyk, J. P. Grote, A. Savan, B. R. Shrestha, S. Merzlikin, B. Breitbach, A. Ludwig and K. J. J. Mayrhofer, *Catal. Today*, 2016, **262**, 170–180.
7 M. Shalom, D. Ressnig, X. Yang, G. Clavel, T. P. Fellinger and M. Antonietti, *J. Mater. Chem. A*, 2015, **3**, 8171–8177.
8 M. G. Walter, E. L. Warren, J. R. McKone, S. W. Boettcher, Q. Mi, E. A. Santori and N. S. Lewis, *Chem. Rev.*, 2010, **110**, 6446–6473.
9 L. Zhuang, L. Ge, Y. Yang, M. Li, Y. Jia, X. Yao and Z. Zhu, *Adv. Mater.*, 2017, **29**, 1606793.
10 M. Tahir, L. Pan, F. Idrees, X. Zhang, L. Wang, J. J. Zou and Z. L. Wang, *Nano Energy*, 2017, **37**, 136–157.
11 L. A. Stern, L. Feng, F. Song and X. Hu, *Energy Environ. Sci.*, 2015, **8**, 2347–2351.
12 P. W. Menezes, C. Panda, S. Loos, F. Bunschei-Bruns, C. Walter, M. Schwarze, X. Deng, H. Dau and M. Driess, *Energy Environ. Sci.*, 2018, **11**, 1287–1298.
13 J. Tian, J. Chen, J. Liu, Q. Tian and P. Chen, *Nano Energy*, 2018, **48**, 284–291.
14 Y. Yan, B. Y. Xia, B. Zhao and X. Wang, *J. Mater. Chem. A*, 2016, **4**, 17587–17603.
15 Y. Yan, B. Y. Xia, X. Ge, Z. Liu, A. Fisher and X. Wang, *Chem.–Eur. J.*, 2015, **21**, 18062–18067.
16 X. Zhang, H. Xu, X. Li, Y. Li, T. Yang and Y. Liang, *ACS Catal.*, 2016, **6**, 580–588.
17 F. S. Zhang, J. W. Wang, J. Luo, R. R. Liu, Z. M. Zhang, C. T. He and T. B. Lu, *Chem. Sci.*, 2018, **9**, 1375–1384.
18 K. N. Dinh, P. Zheng, Z. Dai, Y. Zhang, R. Dangol, Y. Zheng, B. Li, Y. Zong and Q. Yan, *Small*, 2018, **14**, 1703257.
19 Y. Hou, M. R. Lohe, J. Zhang, S. Liu, X. Zhuang and X. Feng, *Energy Environ. Sci.*, 2016, **9**, 478–483.
20 Y. Jia, L. Zhang, G. Gao, H. Chen, B. Wang, J. Zhou, M. T. Soo, M. Hong, X. Yan, G. Qian, J. Zou, A. Du and X. Yao, *Adv. Mater.*, 2017, **29**, 1700017.
21 C. Xiao, Y. Li, X. Lu and C. Zhao, *Adv. Funct. Mater.*, 2016, **26**, 3515–3523.
22 L. Yu, H. Zhou, J. Sun, F. Qin, D. Luo, L. Xie, F. Yu, J. Bao, Y. Li, Y. Yu, S. Chen and Z. Ren, *Nano Energy*, 2017, **41**, 327–336.
23 H. Zhang, X. Li, A. Haehnel, V. Naumann, C. Lin, S. Azimi, S. L. Schweizer, A. W. Maijenburg and R. B. Wehrspohn, *Adv. Funct. Mater.*, 2018, **28**, 1706847.
24 W. Zhu, T. Zhang, Y. Zhang, Z. Yue, Y. Li, R. Wang, Y. Ji, X. Sun and J. Wang, *Appl. Catal., B*, 2019, **244**, 844–852.
25 F. Song and X. Hu, *Nat. Commun.*, 2014, **5**, 4477.
26 S. Anantharaj, K. Karthick and S. Kundu, *Materials Today Energy*, 2017, **6**, 1–26.
27 J. X. Feng, H. Xu, Y. T. Dong, S. H. Ye, Y. X. Tong and G. R. Li, *Angew. Chem.*, 2016, **128**, 3758–3762.
28 Y. Jia, L. Zhang, G. Gao, H. Chen, B. Wang, J. Zhou, M. T. Soo, M. Hong, X. Yan, G. Qian, J. Zou, A. Du and X. Yao, *Adv. Mater.*, 2017, **29**, 1700017.
29 L. Yu, H. Zhou, J. Sun, F. Qin, F. Yu, J. Bao, Y. Yu, S. Chen and Z. Ren, *Energy Environ. Sci.*, 2017, **10**, 1820–1827.
30 L. Yu, H. Zhou, J. Sun, I. K. Mishra, D. Luo, F. Yu, Y. Yu, S. Chen and Z. Ren, *J. Mater. Chem. A*, 2018, **6**, 13619–13623.
31 C. a. Zhou, X. Xia, Y. Wang, Y. Zhong, Z. Yao, X. Wang and J. Tu, *J. Mater. Chem. A*, 2017, **5**, 1394–1399.
32 S. Kandambeth, V. Venkatesh, D. B. Shinde, S. Kumari, A. Halder, S. Verma and R. Banerjee, *Nat. Commun.*, 2015, **6**, 6786.
33 Z. Lu, W. Xu, W. Zhu, Q. Yang, X. Lei, J. Liu, Y. Li, X. Sun and X. Duan, *Chem. Commun.*, 2014, **50**, 6479–6482.
34 Z. Qiu, C. W. Tai, G. A. Niklasson and T. Edvinsson, *Energy Environ. Sci.*, 2019, **12**, 572–581.

 This journal is © The Royal Society of Chemistry 2019

35 X. Ge, C. Gu, Z. Yin, X. Wang, J. Tu and J. Li, *Nano Energy*, 2016, **20**, 185–193.
36 J. J. Lv, J. Zhao, H. Fang, L. P. Jiang, L. L. Li, J. Ma and J. J. Zhu, *Small*, 2017, **13**, 1700264.
37 X. Ge, C. D. Gu, X. L. Wang and J. P. Tu, *J. Mater. Chem. A*, 2014, **2**, 17066–17076.
38 J. L. Gunjakar, B. Hou, A. I. Inamdar, S. M. Pawar, A. T. A. Ahmed, H. S. Chavan, J. Kim, S. Cho, S. Lee, Y. Jo, S. J. Hwang, T. G. Kim, S. Cha, H. Kim and H. Im, *Small*, 2018, **14**, 1703481.
39 M. F. Chiang and T. M. Wu, *Appl. Clay Sci.*, 2011, **51**, 330–334.
40 P. Li, X. Duan, Y. Kuang, Y. Li, G. Zhang, W. Liu and X. Sun, *Adv. Energy Mater.*, 2018, **8**, 1703341.
41 X. Han, C. Yu, J. Yang, C. Zhao, H. Huang, Z. Liu, P. M. Ajayan and J. Qiu, *Adv. Mater. Interfaces*, 2016, **3**, 1500782.
42 S. Yin, W. Tu, Y. Sheng, Y. Du, M. Kraft, A. Borgna and R. Xu, *Adv. Mater.*, 2018, **30**, 1705106.
43 J. Yu, G. Cheng and W. Luo, *J. Mater. Chem. A*, 2017, **5**, 11229–11235.
44 Y. Zheng, Y. Jiao, M. Jaroniec and S. Z. Qiao, *Angew. Chem., Int. Ed.*, 2015, **54**, 52–65.
45 Y. H. Li, P. F. Liu, L. F. Pan, H. F. Wang, Z. Z. Yang, L. R. Zheng, P. Hu, H. J. Zhao, L. Gu and H. G. Yang, *Nat. Commun.*, 2015, **6**, 8064.
46 Y. Jin, S. Huang, X. Yue, H. Du and P. K. Shen, *ACS Catal.*, 2018, **8**, 2359–2363.
47 Y. Wang, M. Qiao, Y. Li and S. Wang, *Small*, 2018, **14**, 1800136.

Published on 31 July 2019. Downloaded on 10/11/2019 5:51:56 AM.